Sensors & Actuators: B. Chemical 313 (2020) 128001

Contents lists available at ScienceDirect

Sensors and Actuators B: Chemical

journal homepage: www.elsevier.com/locate/snb

Rb_2CO_3-decorated In_2O_3 nanoparticles for the room-temperature detection of sub-ppm level NO_2

Nguyen Manh Hung[a,b], Nguyen Minh Hieu[a], Nguyen Duc Chinh[a], Truong Thi Hien[a], Nguyen Duc Quang[a], Sutripto Majumder[a], GyuSeok Choi[c], Chunjoong Kim[a,*], Dojin Kim[a,*]

[a] Department of Materials Science and Engineering, Chungnam National University, Daejeon, 34134, Republic of Korea
[b] Department of Materials Science and Engineering, Le Quy Don Technical University, Hanoi, 100000, Viet Nam
[c] Gumi Electronic and Information Technology Research Institute, Gumi, Gyeongbuk, 39171, Republic of Korea

ARTICLE INFO

Keywords:
Rb_2CO_3/In_2O_3
Room temperature sensor
Light illumination
NO_2 sensing

ABSTRACT

The Rb_2CO_3-decorated In_2O_3 sensor is prepared for detection of NO_2 at room temperature under light irradiation. Physical and chemical properties of the materials and structures are thoroughly investigated by various analytical tools of scanning electron microscopy, transmission electron microscopy, X-ray diffraction, X-ray photoelectron spectroscopy, and Raman spectroscopy, thereby confirming the formation of the Rb_2CO_3/In_2O_3 p-n junction at the interface. The Rb_2CO_3-decoration effect on In_2O_3 sensor is examined under light irradiation of different wavelengths and intensities. Rb_2CO_3-decoration exhibits much higher sensing performance than pure In_2O_3 sensor, and furthermore, the visible light irradiation improves in the response level and sensing kinetics. The sensor detects less than 100 ppb NO_2. In addition, the Rb_2CO_3-decorated In_2O_3 sensor shows high selectivity, stability, repeatability, and linearity. The ultimate performance of the nanostructured sensor is elucidated by the depletion model of the conduction type gas sensors. The effect of humidity on the sensing performance is also investigated.

1. Introduction

Metal oxide semiconductors-based gas sensors are of great attention owing to their small size, high response, cheap price, and chemical stability [1–4]. The simplest operating-principle of the gas sensors is based on the change of their resistance. Since the change of the resistance is originated from the thermally activated interaction between solid and gas phases at the elevated temperature, these gas sensors are known as chemoresistive gas sensors. However, high operating temperature has limited their use in the detection of explosive or flammable gases, particularly under the hazardous environment. In addition, the large power consumption during sensor operation impedes the application in mobile devices. Furthermore, high temperature can lead to the long-term instability of sensors by degradation of their constituting structure and/or material [4–6]. Therefore, the development of sensors that can operate at room temperature (RT) should be made in timely manner. To achieve this goal, researchers have reported various strategies such as doping with metals [7–9], non-metals [10], functionalization with noble metals [11–13], oxides [14], and the illumination of ultra-violet (UV) or visible light [15–20]. Among them, UV or visible light illumination is considered an effective approach, especially when it is combined with the structural modification [21,22]. It is found that the operating temperature of a chemoresistive gas sensor can be replaced by UV or visible light illumination at low temperature to activate the chemical reactions on the surface of gas-sensing materials [23]. On the other hand, the surface decoration of metals, oxides, or alkaline salts could further enhance the light-assisted gas sensing performance of metal oxide sensors. However, the enhancement mechanism is still unclear, which should be understood to design the high-performance RT sensor.

In_2O_3 is an *n*-type semiconductor oxide, which is a promising candidate material RT gas sensor due to its relatively low resistance and high stability. In_2O_3-based gas sensors have been reported to reveal sensing capabilities at low temperature [24–28]. In the meantime, Yamaura et al. [29] investigated In_2O_3 particles coated with various alkaline salts (Li_2CO_3, K_2CO_3, Na_2CO_3, Rb_2CO_3, Cs_2CO_3) to detect *CO* gas, and found Rb_2CO_3-decoration exhibited the highest *CO* sensing response at 300 °C. The result was explained by the catalytic role of

* Corresponding authors.
E-mail addresses: manhhung.hvktqs@gmail.com (N.M. Hung), cockyhieu@gmail.com (N.M. Hieu), chjnhnd@live.com (N.D. Chinh), anhientruong@gmail.com (T.T. Hien), nguyenducquang0903@gmail.com (N.D. Quang), sutriptomajumdervnit2013@gmail.com (S. Majumder), gschoi@geri.re.kr (G. Choi), ckim0218@cnu.ac.kr (C. Kim), dojin@cnu.ac.kr (D. Kim).

https://doi.org/10.1016/j.snb.2020.128001
Received 25 November 2019; Received in revised form 24 February 2020; Accepted 14 March 2020
Available online 04 April 2020

Rb_2CO_3 on oxidation of the reducing gases. However, the sensing properties to oxidizing gases and the effect of p-n junction formation at the Rb_2CO_3/In_2O_3 interface was not examined. The p-n junction formed at the contact of different electronic materials can greatly alter the conductance, and in turn, the sensing performance particularly in nanostructures [24,30,31].

Besides, visible light illumination was proven to be a potential solution to reduce the response and recovery times of the metal oxide-based sensor particularly at low temperatures. From these perspectives, it is attractive to study the combined effect of Rb_2CO_3 decoration and light illumination on the sensing properties of In_2O_3 nanostructure with varying p-n junction properties. In this study, we report that Rb_2CO_3-decorated In_2O_3 structure exhibits a high response to ppb level NO_2 gas at RT (25 °C). The sensor also revealed high selectivity, stability, and linearity toward NO_2 under visible light irradiation. We discuss in detail the Rb_2CO_3/In_2O_3 pn junction that is built at the interface and determines the sensor response level.

2. Experimental section

2.1. Materials

The chemical reagents of rubidium carbonate (Rb_2CO_3, ≥ 99 %) and indium (III) chloride ($InCl_3$, ≥ 98 %) were purchased from Sigma-Aldrich Co., Ltd (USA). The absolute ethyl alcohol (C_2H_5OH, 99.5 %) and ammonia solution (NH_4OH, 28.0 ~ 30.0 %) were supplied by Samchun pure chemical Co., Ltd (Korea). All received reagents were used without any purification.

2.2. Synthesis of In_2O_3 powder and Rb_2CO_3-decorated In_2O_3 powder

In_2O_3 was synthesized by a co-precipitation method as reported elsewhere [32]. In brief, 1 g $InCl_3$ was dissolved into 20 ml deionized (DI) water and stirred until the solution became transparent. The $InCl_3$ and NH_4OH solutions were slowly dropped into 50 ml DI water under the vigorous stirring. The pH of the solution was maintained at pH = 9 by adjusting the amount of NH_4OH during precipitation of $In(OH)_3$. The precipitate was collected by centrifugation followed by washing with DI water and absolute ethyl alcohol several times. The precipitate was dried overnight in an oven at 70 °C and heat-treated in a furnace at 800 °C for 5 h in the ambient atmosphere, finally yielding the yellow In_2O_3 particles. In order to finely distribute Rb_2CO_3 on the In_2O_3 particles, each 0.2 g In_2O_3 was impregnated in a 10 ml Rb_2CO_3 aqueous solution with different concentrations and then dried in air for 24 h. Finally, the Rb_2CO_3-decorated In_2O_3 (Rb_2CO_3/In_2O_3) particles were harvested. Pure In_2O_3 was labeled as A0 while Rb_2CO_3/In_2O_3 powders decorated in different concentrations (0.01 M, 0.02 M, 0.04 M, and 0.08 M) of Rb_2CO_3 solutions were labeled as A1, A2, A3, and A4, respectively. Before characterization and examination of the powders, they were annealed at the same conditions for the sensors fabrication.

2.3. Materials characterizations

The surface morphology and microstructure of the synthesized In_2O_3 and Rb_2CO_3/In_2O_3 were investigated by field-emission electron scanning microscopy (FE-SEM, JSM 700 F, JEOL, Japan) and transmission electron microscopy (TEM, JEM-ARM 200 F, JEOL, Japan). Energy dispersive spectroscopy (EDS) equipped with SEM and TEM were used to examine the elemental distribution. Crystalline structures were analyzed by X-ray diffraction (XRD, X'pert PRO-MPD, PANalytical, Netherlands) with Cu Kα radiation (λ = 0.15418 nm). X-ray photoelectron spectroscopy (XPS, VG Multilab 2000, Thermo VG Scientific, UK) measurement was also conducted to determine the chemical states of elements. The chemical structures were examined by using Raman spectroscopy at a 532 nm wavelength at room temperature using SR 303i laser source (Andor Technology Ltd, Oxford Instrument, UK). Photoluminescence (PL) was recorded with an excitation wavelength of 325 nm at room temperature using a PL spectrophotometer (LabRAM-HR 800, Horiba Jobin Yvon Ltd, Japan). The surface area of the particulate sensor structures was measured by the Brunauer-Emmett-Teller (BET) method in which the N_2 adsorption-desorption measurement was conducted on a 3Flex analyzer (ASAP 2420, Micormeritics Instrument Corp., US) for the samples outgassed at 200 °C for 5 h before the measurements.

2.4. Sensors fabrication and gas sensing property measurements

Alumina substrates patterned with interdigitated comb-type gold electrodes were used to fabricate sensors. The In_2O_3 or Rb_2CO_3/In_2O_3 particles were thoroughly mixed with a suitable amount of ethyl alcohol to form a slurry and pasted onto the alumina substrate using the bar-coating method (Fig. S1a, Supporting Information). Casted sensor structures were dried in air for 2 h, followed by heat-treatment in a furnace at 500 °C for 5 h in the air to the intimate contact among In_2O_3 and/or Rb_2CO_3 particles as well as the adhesion of gas-sensing materials to the electrode.

The gas-sensing measurement setup is illustrated in Fig. S1b, Supporting Information. The total 400 sccm gas flow rate including NO_2 analyte gas was controlled by the mass flow controller (MFC). Response (S) of the sensor was determined by $S = R_g/R_a$ for oxidizing gases and $S = R_a/R_g$ for the reducing gases, where R_a and R_g are the resistance values of the sensor under the flowing of the dry air and target gas, respectively. The response and recovery times were also estimated assuming exponential rise and decay of the response and recovery cycles of the sensing, respectively, which based on the Langmuir adsorption model. The specific calculations can be found in our previous reports [33,34]. Therefore, the response time corresponds to the time to reach ~63 % of the saturated response level, and similarly, the recovery time is for ~63 % decay from the response level. The response and recovery times are based on the physics model of the surface processes, which are different from the corresponding engineering estimation of the times, or 90 % of the final values.

To investigate the effect of light irradiation on the gas-sensing properties at RT, light-emitting diodes (LEDs) with various wavelengths, red (625 nm), dark-green (460 nm), and blue (439 nm) were used. The sensor was illuminated by LEDs at a fixed distance from the outside of the measurement chamber through a quartz window. The light illumination intensity (I) was estimated using the equation $I = P/4\pi r^2$ [μW/cm^2], where P is an illuminating power from the LED source and r is the distance from LED to the sensor. In order to examine the humidity effect, dry air was flown through a water bubbler to prepare water-saturated gas of 100 % humidity. A MFC controlled the ratio between wet and dry air flow, thereby monitoring the relative humidity. The relative humidity values in the gas sensing measurement chamber were confirmed by an external commercial humidity sensor (Testo 635, Germany).

3. Results and discussion

3.1. Structural and morphological characteristics

SEM images of In_2O_3 and Rb_2CO_3/In_2O_3 powders are presented in Fig. 1a to e. All the In_2O_3 and Rb_2CO_3/In_2O_3 powders revealed morphology of aggregated particles of ~40 nm diameter. No remarkable apparent change in the particle size and morphology could be seen by coating of Rb_2CO_3 at different concentrations, but BET measurements revealed that the surface area of the structure slightly decreased with Rb_2CO_3 coating as will be shown later. Furthermore, we think the Rb_2CO_3 cluster (as shown by TEM) sizes coated on the In_2O_3 particle surface will increase with the concentration of the Rb_2CO_3 solution. The overall thicknesses of the sensor body of agglomerated particulates were in the range of 2–4 μm as shown by the SEM images (Fig. S2,

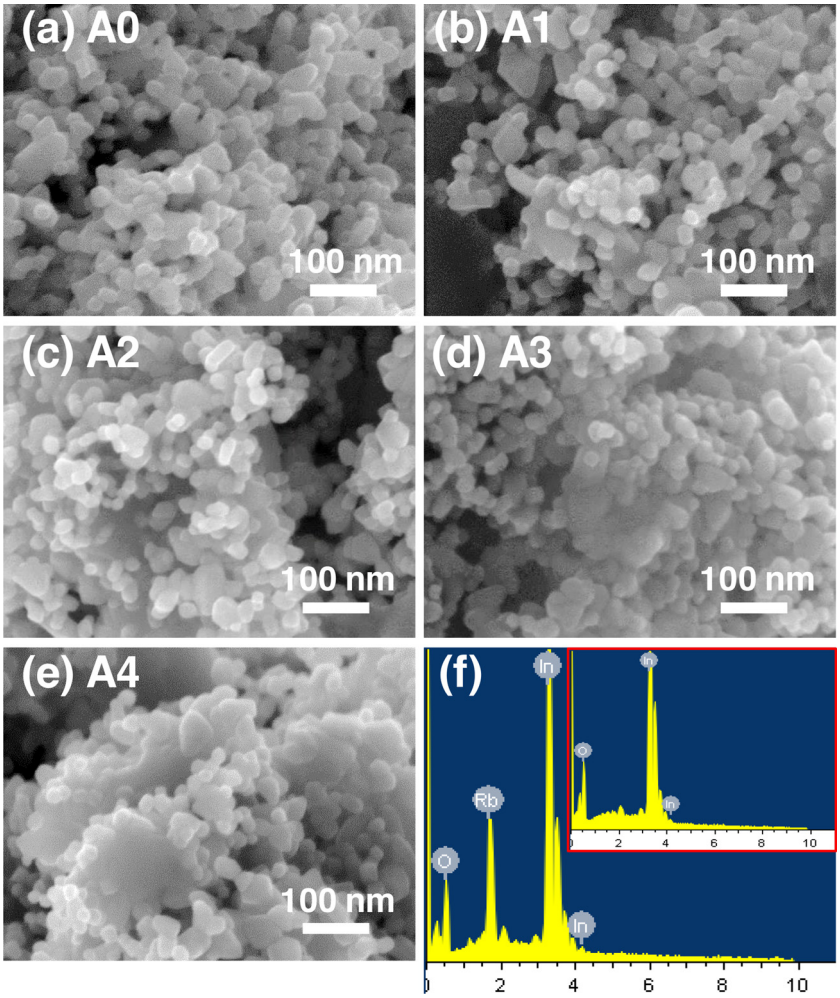

Fig. 1. SEM images of (a) pristine In_2O_3 (A0) and (b-e) Rb_2CO_3/In_2O_3 powders with different concentrations of Rb_2CO_3: (b) A1 (0.01 M), (c) A2 (0.02 M), (d) A3 (0.04 M), and (e) A4 (0.08 M). (f) EDS spectrum of A2 powder compared with that of pristine In_2O_3 in the inset.

Supporting Information). The EDS spectra comparison between pristine In_2O_3 and Rb_2CO_3/In_2O_3 clearly confirmed the presence of Rb element coated (Fig. 1f). All the examinations of the Rb_2CO_3/In_2O_3 sample in this study are A2 unless specified.

The XRD patterns of In_2O_3, Rb_2CO_3, and Rb_2CO_3/In_2O_3 (A2 sample) are shown in Fig. 2a. The strong diffraction peaks of the cubic phase In_2O_3 were observed at (211), (222), (400), (134), and (440) lattice planes (JCPDS 89-4595). The Debye-Scherrer analysis of the (222) peak estimated the particle size of 43 nm (Fig. S3, Supporting Information), which matches that observed in the SEM images.

The XRD pattern of Rb_2CO_3/In_2O_3 exhibited the additional peaks of (102), (200), (112), and (103) crystalline planes for Rb_2CO_3 [35]. While the XRD patterns confirmed the crystalline Rb_2CO_3 existing in Rb_2CO_3/In_2O_3 particles, no other crystalline phases could be observed. Fig. 2b displays the Raman spectra of Rb_2CO_3, In_2O_3, and In_2O_3/Rb_2CO_3. In_2O_3 showed the characteristic peaks at 131, 205, 303, 366, 495, and 628 cm^{-1} [36,37]. The strongest peak at 1050 cm^{-1} with small harmonic peaks at 72, 102, 130, 151, and 680 cm^{-1} were ascribed to

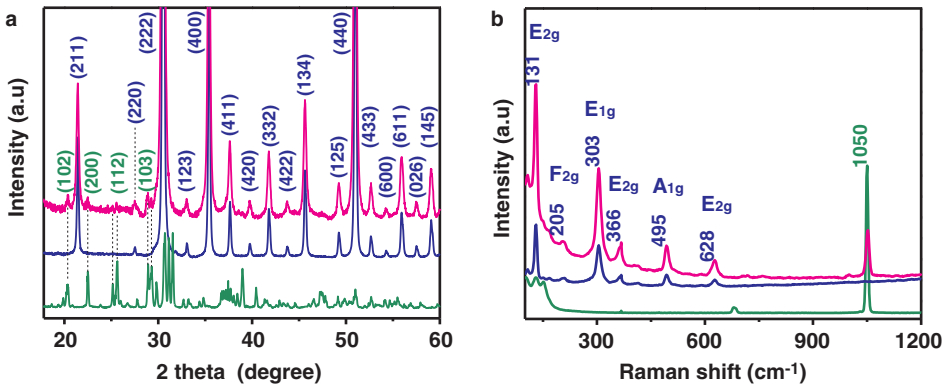

Fig. 2. X-ray diffraction and Raman spectra of Rb_2CO_3 (green), In_2O_3 (blue) and In_2O_3/Rb_2CO_3 (pink) (For interpretation of the references to colour in this figure legend, the reader is referred to the web version of this article.).

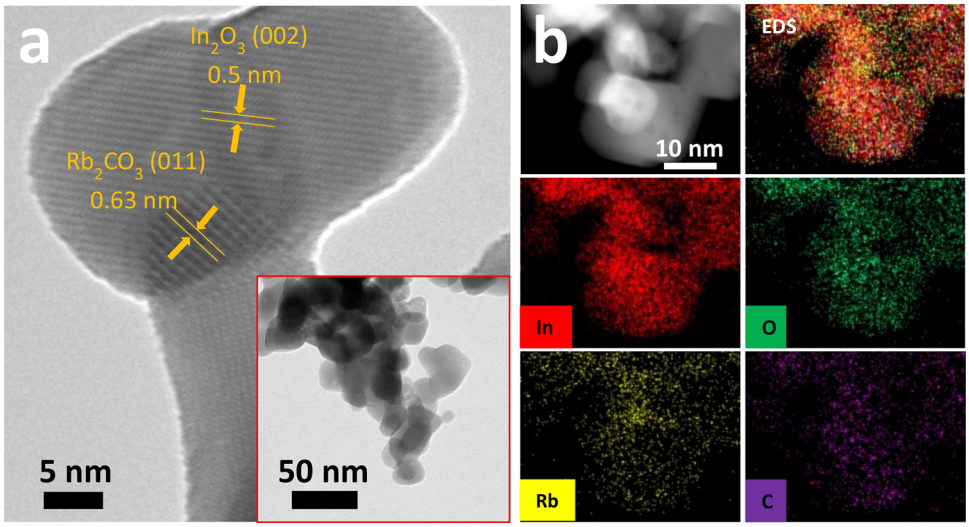

Fig. 3. (a) HRTEM lattice image of Rb_2CO_3/In_2O_3 particle with insert showing the TEM image of the particles. (b) TEM and EDS of Rb_2CO_3/In_2O_3 with elemental mapping images showing the distribution of In, O, Rb, and C elements.

Rb_2CO_3 [38]. In the In_2O_3/Rb_2CO_3, the peak 1050 cm^{-1} was observed, which indicates the existence of Rb_2CO_3 phase in the structure as well. The HRTEM image of the In_2O_3/Rb_2CO_3 (Fig. 3a) and the corresponding fast Fourier transformation (Fig. S4, Supporting Information) further confirmed the high-quality crystalline phases of In_2O_3 and Rb_2CO_3 as presented by 0.5 nm (002) lattice plane of In_2O_3 and 0.63 nm (011) lattice plane of Rb_2CO_3. The EDS mapping taken from the Rb_2CO_3/In_2O_3 showed a uniform distribution of Rb element, suggesting the formation of $RbCO_3$ clusters distributed on In_2O_3 particles (Fig. 3b).

The chemical bonding natures were examined by XPS (Fig. 4). The survey spectra of Rb_2CO_3, In_2O_3, and Rb_2CO_3/In_2O_3 showed no impurity peaks other than In, Rb, O, and C (Fig. 4a). High-resolution XPS spectra of In 3*d* core-level (Fig. 4b) exhibit the binding energies at 444.33 and 451.85 eV, which were ascribed to In $3d_{5/2}$ and In $3d_{3/2}$ orbitals of the In^{3+} state, respectively [39]. In the meantime, the binding energies of In in the Rb_2CO_3/In_2O_3 structure were slightly shifted down to 443.4 and 450.79 eV compared to those of the pristine In_2O_3. The low energy shift resulted from the electron donation from Rb to In since Rb_2CO_3 is one of the most electropositive alkaline metals. The doublet from the Rb 3d core level of pure Rb_2CO_3 is also shown in Fig. 4c, which matches Rb $3d_{3/2}$ (110.69 eV) and Rb $3d_{5/2}$ (109.22 eV). In the XPS spectra of Rb, the Rb^+ state exists in Rb_2CO_3 [39], of which binding energies were slightly shifted upward in Rb_2CO_3/In_2O_3 as contrary to the observation in indium. The chemical compositions on the surface of the Rb_2CO_3/In_2O_3 were estimated from the XPS spectrum, which showed the Rb concentration in Rb_2CO_3/In_2O_3 as 4.69 at %. (Table S1, Supporting Information).

The up- and down-shifts of the In and Rb binding energies in Rb_2CO_3/In_2O_3, respectively, compared to their pure counterparts can be explained by the formation of p-n junction at the Rb_2CO_3/In_2O_3 interface. When a p-n junction is formed between a p-type Rb_2CO_3 and an n-type In_2O_3, the positive charges in the space charge region of the In_2O_3 side will increase the electron binding energy, whereas the negative charges in the space charge region of the Rb_2CO_3 side will decrease that [29,39,40]. The dramatic increase in the resistance by the decoration of Rb_2CO_3 onto the In_2O_3 sensor, as will be discussed later, is led by the formation of the p-n junction at the interface between Rb_2CO_3 and In_2O_3 particles. It should be noted that the radius of Rb^+ (148 pm [41]) is much larger than that of In^{3+} (62 pm [42]), thus, effective doping of Rb into the In_2O_3 lattice is difficult to occur. Therefore, the deposition of small Rb_2CO_3 islands or clusters on the In_2O_3 particles forms the Rb_2CO_3/In_2O_3 interface leading to a p-n junction formation.

3.2. Gas sensing properties

Dynamic change in the resistance of In_2O_3 and Rb_2CO_3/In_2O_3 sensors during exposure to 250 ppb NO_2 gas (diluted in dry air) were investigated at 25 °C in dark or under the light irradiation with the 439 nm wavelength at an intensity of 160 μW/cm^2 (Fig. 5a). The resistance changes were translated into the sensor response and recovery curves as shown in Fig. 5b and c, which exhibit logarithmic changes of the signals. The response and recovery time constants were calculated in Fig. 5d and e assuming exponential rise and decay of the response

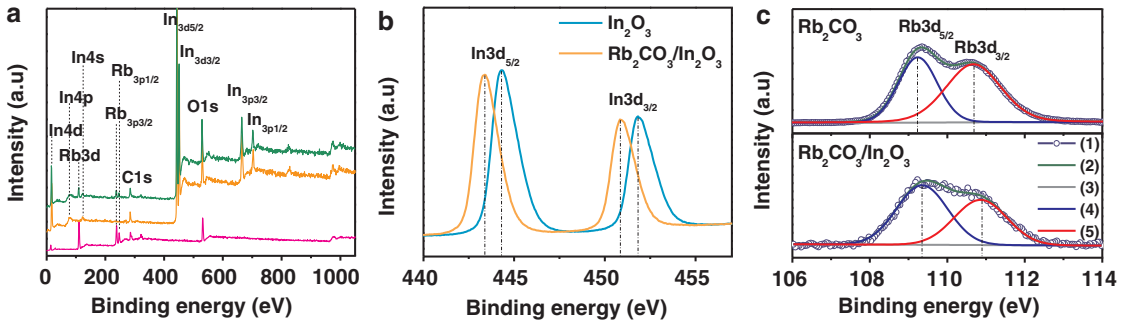

Fig. 4. (a) Survey XPS spectra of Rb_2CO_3 (pink), In_2O_3 (yellow), and Rb_2CO_3/In_2O_3 (green). High-resolution spectra of (b) In 3d and (c) Rb 3d: (1) Experiment curves, (2) Fitted curves, (3) Baseline, (4) Peak 1, and (5) Peak 2. XPS spectra of In 3d and Rb 3d showed opposite side shifts by heterojunction formation (For interpretation of the references to colour in this figure legend, the reader is referred to the web version of this article.).

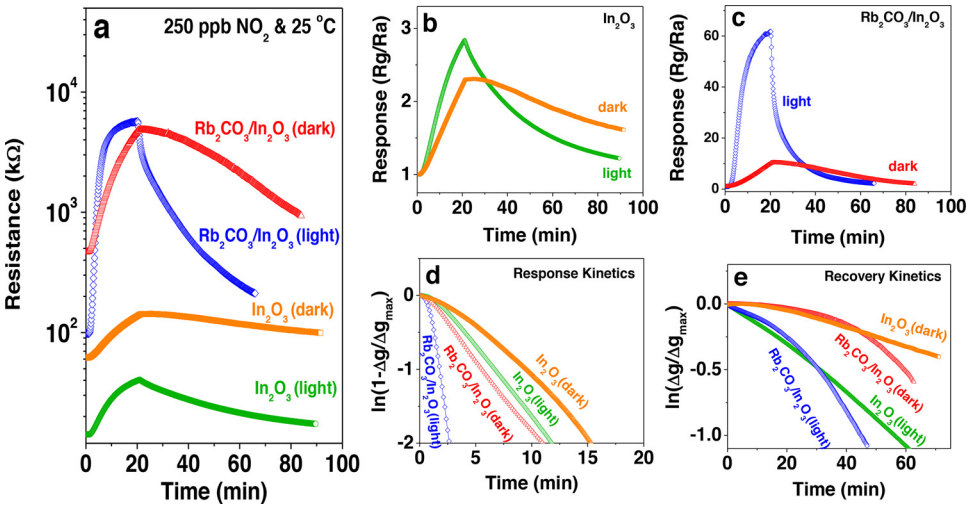

Fig. 5. (a) Resistance change of the sensors to 250 ppb NO_2 gas at 25 °C in dark or under irradiation of 439 nm light at the intensity of 160 μW/cm^2: In_2O_3 in dark (orange) and under the light (green) and Rb_2CO_3/In_2O_3 (A2) in dark (red) and under the light (blue). Response plots for (b) In_2O_3 and (c) Rb_2CO_3/In_2O_3 (A2). Plots of (d) response time and (e) recovery time assuming exponential rise and decay behaviors of the response and recovery kinetics [33,34] (For interpretation of the references to colour in this figure legend, the reader is referred to the web version of this article.).

and recovery curves [33,34]. Our observations can be summarized as the following:

i) The resistance of In_2O_3 (~60 kΩ) increased by eight times upon the decoration of Rb_2CO_3 (~500 kΩ).
ii) The sensor response of the Rb_2CO_3/In_2O_3 sensor was higher than that of the In_2O_3 sensor in dark (10 vs. 2.3) and under the light (60 vs. 2,8).
iii) The light irradiation resulted in a higher sensing response level, particularly in the Rb_2CO_3/In_2O_3 sensor.
iv) Both of the response and recovery kinetics were enhanced by the light irradiation

The pristine In_2O_3 exhibiting a relatively low resistance (~60 kΩ in dark as shown in Fig. 5a) has a relatively large intrinsic n-type defects, which will lead to a relatively thin depletion depth. The cross-section of the particle was accordingly sketched in Fig. 6a showing a large neutral region in the center. The increase of the depletion region depth is also relatively small even with adsorption of a high concentration NO_2. The condition results in a small modulation of the depletion region depth (or small $\Delta R = R_g - R_a$) leading to a poor sensing signal or small $S = R_g/R_a$ (as shown in Fig. 5b). The light irradiation causing an increased electron-hole-pairs (EHPs) in In_2O_3 exhibited only a small effect on the sensing signal level (Fig. 5b). In this case, the neutral core size in Fig. 5a was further increased (smaller R_a), but at the same time, the added photo-carriers enhanced the NO_2 molecular adsorption rate on the surface via fluent electrons supply to the surface to increase the depletion depth. The net results are the slightly increased response level and response rate, as shown in Fig. 5b [14,43].

On the other hand, the enhanced response level in the Rb_2CO_3/In_2O_3 structure in dark is attributed to the greatly reduced conduction region in the In_2O_3 particles caused by the Rb_2CO_3/In_2O_3 p-n junction

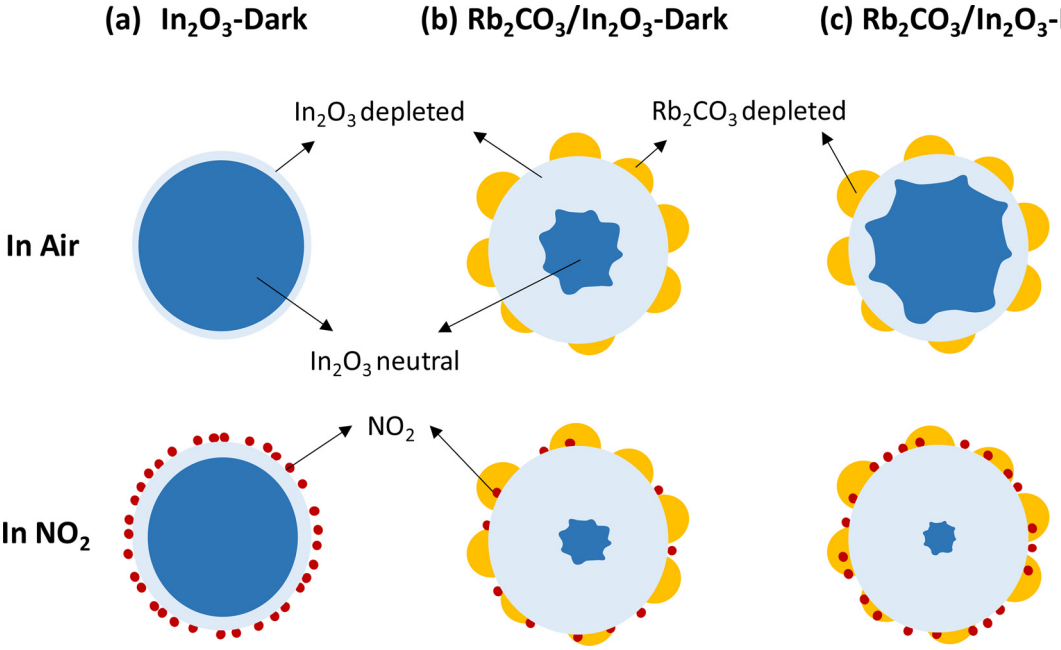

Fig. 6. Schematic illustration of the sensor particles in different conditions. (a) Bare In_2O_3 in dark showing narrow depletion depth in air under O_2 adsorption due to the high intrinsic doping level. The NO_2 adsorption rate may high, but the depletion depth increase is relatively small. (b) Rb_2CO_3/In_2O_3 in dark exhibits a highly expanded depletion depth owing to the p-n junction formation, and the junction further expands with NO_2 adsorption. A far less NO_2 adsorption compared to the case (a) can lead to a higher response level. (c) Rb_2CO_3/In_2O_3 under the light in air. The photo-carriers narrowed the depletion depth, but increase the NO_2 adsorption rate leading to a higher modulation of the depletion depth.

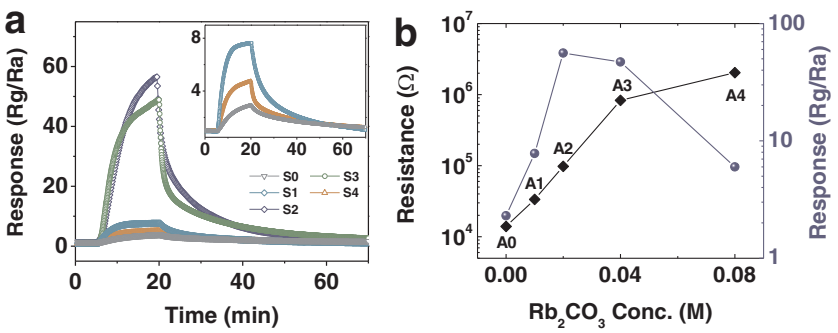

Fig. 7. (a) Response-recovery curves of In_2O_3 and Rb_2CO_3/In_2O_3 sensors toward 250 ppb NO_2 under 439 nm light illumination at 25 °C. The insert shows a magnification of the low-response curves. (b) The base resistance monotonically increased with the Rb_2CO_3 content while the response level showed the peak at 0.02 M Rb_2CO_3.

formation. This is proven by the eight times increased R_a in the Rb_2CO_3/In_2O_3 structure (~500 kΩ in dark in Fig. 5a) compared with that in the bare In_2O_3. Such condition in the Rb_2CO_3/In_2O_3 structure is sketched in Fig. 6b, which is characterized by a far decreased cross-section area of the neutral core (or a far increased depletion depth) compared with the bare In_2O_3. Now R_g is determined by the adsorption rate of NO_2 molecules on the surface, and which is also determined by the rate of electrons supply from the neutral core to the surface, as repeatedly discussed in our previous studies [23,33,34,44,45]. The NO_2 adsorption rate onto In_2O_3 surface may be smaller in the Rb_2CO_3/In_2O_3 due to Rb_2CO_3 coating. However, as indicated in Fig. 6b, a smaller NO_2 adsorption rate can cause a greater depletion depth modulation because of the initially smaller neutral core or higher R_a. As a result, a far increased R_g in the Rb_2CO_3/In_2O_3 could lead to the high response (S ~ 10 in Fig. 5c).

The light shining on the Rb_2CO_3/In_2O_3 structure reduce the resistance with the added photo-generated EHPs (~90 kΩ in Fig. 5a), but the resistance is still higher than the bare In_2O_3 in dark. Therefore, the depletion depth is greater than the In_2O_3 in dark and smaller than the Rb_2CO_3/In_2O_3 in dark. This condition is sketched in Fig. 6c. The light irradiation on one hand narrows the depletion depth with the increased electron concentration, and the other hand increases the electron supply rate to the surface leading to enhancement of the NO_2 adsorption rate. The higher NO_2 adsorption rate under the light is sketched in Fig. 6c and is supported by the response and recovery times measurements in Fig. 5d and 5e. Note that the enhanced adsorption rate of NO_2 causes a core neutral region even smaller than that in the Rb_2CO_3/In_2O_3 in dark as supported by the response level of the Rb_2CO_3/In_2O_3 under the light (~6 MΩ in Fig. 5a) which is slightly greater than that in dark (~5 MΩ in Fig. 5a). Therefore, the charge modulation (or equivalently $\Delta R = R_g - R_a$) was much greater under the light than in dark, which led to the greatly enhanced response signal (S ~ 60), as depicted in Fig. 5c. Therefore, we could explain the enhanced response signal of Rb_2CO_3/In_2O_3 under the light compared that in dark using the conduction model for nanostructured sensors based on the sensing signal measurement data.

Fig. 5d and e present the response and recovery kinetics of the In_2O_3 and Rb_2CO_3/In_2O_3 sensors in dark and under the light. They showed another prominent effect of light illumination, which is the enhancement in sensing kinetics. Because both adsorption and desorption of the molecules on the oxide surface are the thermally activated processes, the supply of enough photon energy to the gas molecules to overcome the adsorption barrier energy as well as to the adsorbed molecules to overcome the desorption barrier energy accelerate the overall kinetics in adsorption and desorption processes. This is equivalent to say that the supply of higher carrier concentration to the surface enhances the adsorption and desorption kinetics. The faster response times were observed both in dark and light illumination by the Rb_2CO_3 decoration as shown in Fig. 5d. While the response times of In_2O_3 were ~16 and ~12 min in dark and under the light, respectively, those of Rb_2CO_3/In_2O_3 were ~11 and ~2.5 min, respectively. The enhanced adsorption kinetics with Rb_2CO_3 decoration in dark and under the light can be explained by a catalytic effect of Rb_2CO_3 on the adsorption of NO_2, which enables facile adsorption of NO_2 on the In_2O_3 at the vicinity of Rb_2CO_3 [23,29]. The light irradiation further enhanced the response kinetics by the enhanced electron supplying rate to the adsorbing NO_2 on the In_2O_3 surface. Enhanced desorption kinetics were also confirmed under the light for both In_2O_3 and Rb_2CO_3/In_2O_3 structures owing to an enhanced desorption rate of NO_2 and/or enhanced adsorption rate for O_2^- (Fig. 5e). Note in Fig. 5e that the desorption rate for NO_2^- and/or adsorption rate for O_2^- were not influenced strongly by Rb_2CO_3 both in dark and under the light. The results suggest that the catalytic effect of Rb_2CO_3 is negligible in the processes of the desorption of NO_2^- and/or adsorption of O_2^-.

To further clarify the role of Rb_2CO_3 decoration, NO_2 sensing property was examined with varying the content of Rb_2CO_3 clusters deposited on In_2O_3 particles. The specific surface area changing with the Rb_2CO_3 concentration was measured by the BET method and compared between A0 and A2 samples (Fig. S5, Supporting Information). The BET surface area was slightly smaller with Rb_2CO_3 decoration possibly from an increased particle sizes in average. Fig. 7a shows the dynamic response-recovery curves of In_2O_3 and Rb_2CO_3/In_2O_3 (A0 to A4 samples) to 250 ppb NO_2 under the light illumination, and the response levels and base resistances of the samples are summarized in Fig. 7b. The resistance monotonically increased with the Rb_2CO_3 concentration indicating that the p-n junction depletion depth has increased with increase of the content of Rb_2CO_3 clusters on the In_2O_3 particles. The response showed the maximum with 0.02 M Rb_2CO_3 concentration and decreased at higher concentrations. The latter observation can be explained by the increasing depletion depth in the In_2O_3 particles owing to the increasing volume of the Rb_2CO_3 clusters. Namely the condition approaches from Fig. 6c to b with increasing the volume of Rb_2CO_3. As such, the observed sensing responses can be explained by the p-n junction formation. The declining response at higher Rb_2CO_3 concentration could be further affected by the reduced NO_2 absorption site density on the In_2O_3 surface caused by the increasing Rb_2CO_3 coverage.

Meanwhile, the effect of the light illumination with different wavelengths (i.e. different photon energies) on gas sensing properties of Rb_2CO_3/In_2O_3 sensor was also investigated at 25 °C. The resistance changes of the Rb_2CO_3/In_2O_3 sensor under the visible LEDs with wavelengths of 439, 460, and 625 nm is displayed in Fig. 8a. The power intensity was fixed at 160 μW/cm^2. The higher photon energy results in higher photo-generated EHPs showing orders of magnitude decreased sensor resistance. The lowest resistance was measured under the light with a wavelength of 439 nm. The RT gas sensing performances of the Rb_2CO_3/In_2O_3 sensor toward 250 ppb NO_2 gas measured under the light of different wavelengths were shown in Fig. 8b. The remarkable enhancement in sensing response as well as sensing kinetics could be detected under the light with a shorter wavelength than 460 nm. Though its corresponding energy, ~2.70 eV, is smaller than the direct bandgap of In_2O_3 (between 3.1 and 3.9 eV [46–48]), the photon energy is greater than the defect level in In_2O_3. The defect level observed by photoluminescence measurement was estimated to be ~580 nm (Fig.

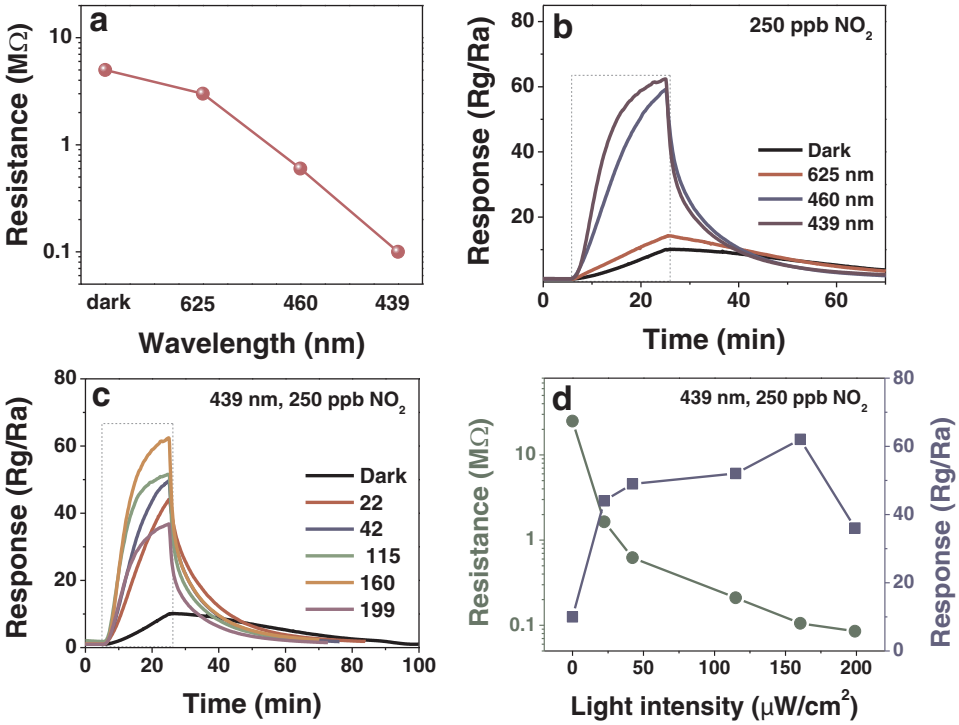

Fig. 8. (a) The resistance changes and (b) sensing performance of the Rb_2CO_3/In_2O_3 sensor toward NO_2 under the illumination of the light with different wavelengths at a fixed light intensity of 160 μW/cm^2. (c) Response-recovery kinetic curves and (d) corresponding resistances and response levels of the Rb_2CO_3/In_2O_3 sensor toward NO_2 with different light intensities.

S6), which coincides with previous studies [49]. Therefore, only a small enhancement in the response level and kinetics were observed under the light of 625 nm. The irradiation of the 439 nm light exhibited the maximum response; thus, this wavelength was kept used in the sensor for further investigation.

The response and recovery curves of the Rb_2CO_3/In_2O_3 sensor at RT under 439 nm radiation with different intensities are presented in Fig. 8c. This experiment was to obtain the light condition for the maximum sensor performance. The response levels were saturated in 20 min at the light intensity higher than 115 μW/cm^2. As summarized in Fig. 8d, the sensor resistance (R_a) continuously decreased with the increase of the light intensity, but R_g will also continuously vary with the varying number of electrons supplied to the surface. The maximum response was obtained at an intermediate intensity of 160 μW/cm^2 (Fig. 8c and d), which is the condition for the highest R_g/R_a. The sensor response enhancement at RT under the light irradiation has been repeatedly reported [50–52], where the light irradiation could supply more electrons on the oxide surface for enhanced adsorption and desorption rates of the gas molecules. Meanwhile, the maximum response with an intermediate light wavelength and/or intensity for the given dimension of the nanostructure sensors could be elucidated by the depletion model of the conduction type gas sensors [23,24,44,53].

The sensing behavior of the Rb_2CO_3/In_2O_3 sensor to different NO_2 concentrations is studied with the same condition above (at 25 °C under 439 nm illumination at the intensity of 160 μW/cm^2). The sensor showed a linear dependence on the NO_2 concentration in the range of examination as shown in Fig. 9a. The raw data are shown by the inset. When the linearity is extended to the x-axis, the detection limit of the sensor defined by $R_g/R_a \sim 3$ was about 80 ppb. The repeatability of the sensor response was also shown in Fig. 9b, which confirms reversibility during sensor operation. The long-term stability of the Rb_2CO_3/In_2O_3 sensor is presented in Fig. 9c showing good stability with the resistance change ± 2% during 45 days. The raw data measured is depicted in Fig. S7. In addition, the selectivity of the sensor was excellent among the gases of SO_2, NH_3, CO, H_2, and CH_4 as shown in Fig. 9d. The selectivity was extremely high with respect to the examined reducing gases as shown by the negligible responses to 100 − 1000 ppm concentrations. The insignificant response to NH_3 with poor recovery was observed under the light (Fig. S8a, Supporting Information). At the low operation temperature, the response signal to NH_3 is due to adsorption rather than the combustion reaction occurring at high temperatures. This led to the poor recovery behavior. Meanwhile, the response to an oxidizing gas, SO_2, was relatively higher than those to the reducing gases and exhibited reasonable desorption in the recovery cycle (Fig. S8b, Supporting Information). However, the response was still far smaller (about 1/30) than that to NO_2. Generally, all observations support that the Rb_2CO_3/In_2O_3 sensor can be further developed to the RT operating NO_2 detection sensor.

Humidity is one of the most critical issues for the RT operating gas sensors. The effect of humidity on gas sensing performance of Rb_2CO_3/In_2O_3 sensor was investigated as summarized in Fig. 10. The sensing condition is the same as the above (i.e. at 25 °C under the 439 nm light at 160 μW/cm^2). With the increase of the relative humidity (RH), the base resistance of the sensor decreases continuously to tens of kilo-ohm via electron donation of water molecules to n-type In_2O_3. However, the flow of 250 ppb NO_2 significantly increased the sensor resistance to mega-ohm ranges (Fig. 10a and b). The response-recovery curves derived by the resistance variation were plotted as shown in the response curves (Fig. 10c). The response levels were further summarized in Fig. 10d. The maximum response level of the sensor was recorded to be ~140 with the sensor resistance 34 kΩ at RH = 45 %, which is far greater than ~65 with the sensor resistance of ~105 kΩ at RH = 0%. The observation can be summarized as the following:

i) The resistance monotonically decreases with RH increase, but the resistance is significantly elevated upon NO_2 flow (Fig. 10b). RH between 30 and 45 % could lead to the enhancement of the sensor response (Fig. 10c).

ii) The humidity effect is small when RH is lower (< 23 %) and the response also shows degradation in higher RH (≥ 62 %).

It is well known that the adsorbed water molecules donate electrons, thereby lowering the resistance of n-type semiconductors [54]. As a result, increased electron concentration in the sensor can further supply the electrons to the adsorbing NO_2 molecules. As we already discussed that the present condition of light intensity (439 nm, 160 μW/cm^2) resulted in the maximum resistance modulation in the dry air condition, the higher electron concentration is expected to lower the

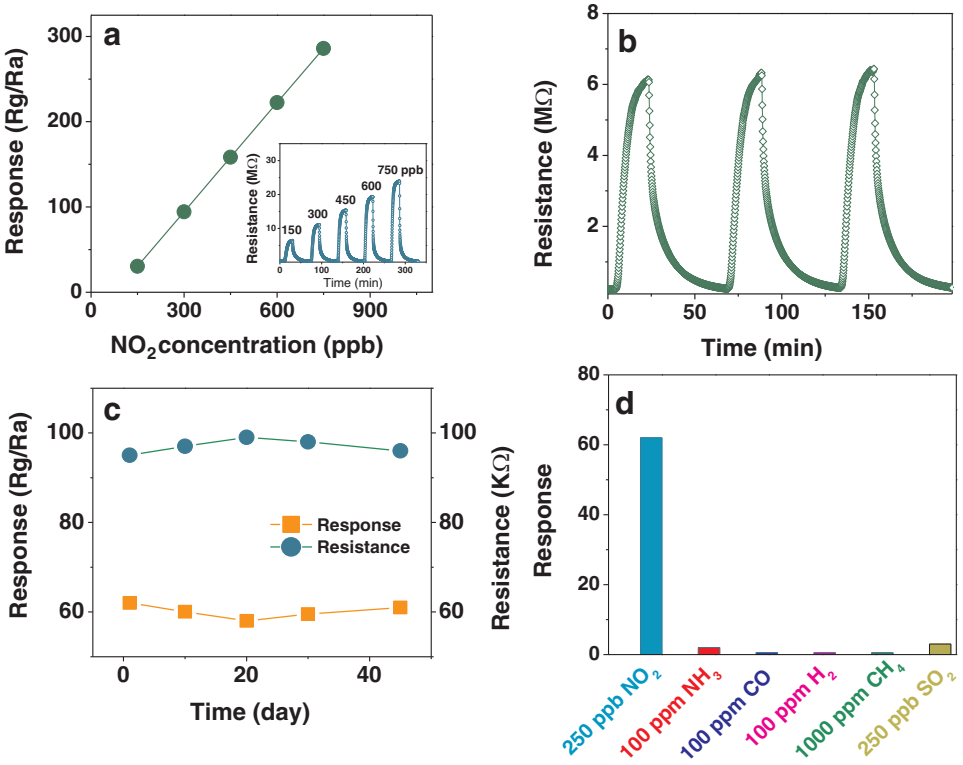

Fig. 9. The Rb_2CO_3/In_2O_3 sensor properties measured under 439 nm/160 μW/cm^2 intensity radiation at 25 °C. (a) The linearity of the sensor with the response-recovery curves for different NO_2 concentrations shown by the inset. (b) The repeatability of the sensor measured with 150 ppb NO_2 and (c) long-term stability of the resistance and response levels. (d) The selectivity of the NO_2 gas sensor in comparison with NH_3, CO, H_2, CH_4, and SO_2.

resistance followed by a decrease in sensing response (Fig. 8d). Interestingly, while the increase of the electron concentration by light illumination degraded the sensing response, that by humidity enhanced the sensing response. Therefore, the great response enhancement to ~140 by humidity cannot result from the increased electron supply from the sensor body.

Rather than that, adsorbed water molecules could affect the gas adsorption reaction in different ways. The NO_2 adsorption on the surface can be enhanced via the surface reaction pathway, surface reactivity and mobility of gas molecules/ions, higher stability of the adsorbed species, etc. It is reported that the water molecules on the oxide surface not only enhanced the surface reaction rate but also the extent

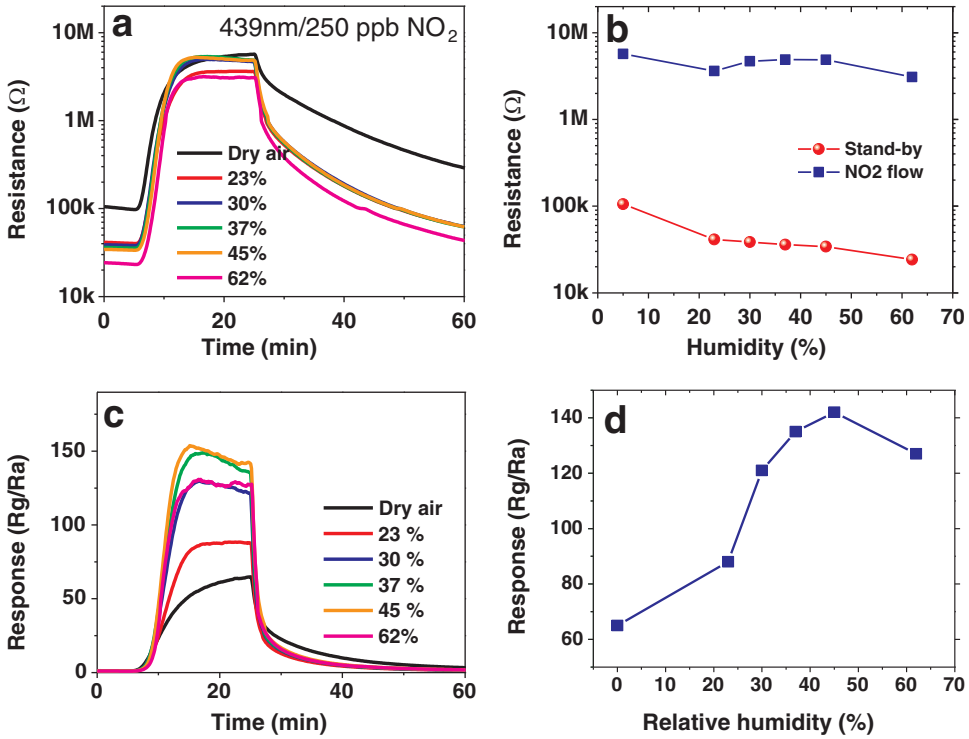

Fig. 10. The response-recovery curves of Rb_2CO_3/In_2O_3 sensor measured at 25 °C with different relative humidity. Plots are given by the (a, b) resistances and (c, d) response level.

of reaction [55]. For NO_2 impingement, water molecules on the oxide surface accelerated NO_2 adsorption reaction via the formation of HNO_3 and/or solvation of nitrate ions, etc. [55,56]. The greatly increased amount of NO_2 adsorption with water molecules can be demonstrated by far increased response with RH between 30–50 % as shown in Fig. 10c and d. The further adsorption of water molecules at higher RH (> 62 %) inhibits the surface reaction by blocking the adsorption sites [55], which can lead to the degraded NO_2 adsorption in Fig. 10c. The rapidly enhanced response rates by the increase of RH are also explained by the humidity effect. As summarized in Fig. 10d, the humidity enhanced the NO_2 sensing response levels. However, the NO_2 gas concentration cannot be accurately estimated under varying humidity in the environment particularly at RT. Therefore, a humidity sensor needs to be implemented in parallel for the RT detection of NO_2 gas [45].

4. Conclusions

In our study, we demonstrated the Rb_2CO_3-decorated In_2O_3 (Rb_2CO_3/In_2O_3) nanostructure for the first time, which can be a promising sensor material to detect NO_2 under the blue light illumination at room temperature. The structure exhibited high sensing performance showing a detection limit of 80 ppb for sensing of NO_2. High sensing response, linearity, reproducibility, selectivity, and long-term stability were confirmed at the room temperature operation. Rb_2CO_3 decoration on In_2O_3 formed a p-n junction at the Rb_2CO_3/In_2O_3 interface. While the p-n junction formation increased the resistance in the In_2O_3 sensor and enhanced sensing performance to NO_2, the light irradiation of 439 nm wavelength further improved the sensing response level and response/recovery kinetics. Our observations could be thoroughly understood by the conduction model in the nano-sized semiconducting sensors, and the enhanced response of the Rb_2CO_3/In_2O_3 sensor was a combined effect of the two: the decreasing conductance of the In_2O_3 transducer owing to the p-n junction formation that influences R_a, and the photo-carriers that facilitate the NO_2 adsorption on the surface and determine R_g. The net consequence was the enhanced response to NO_2. The Rb_2CO_3 decoration also enhanced the NO_2 adsorption kinetics in dark and under the light, but negligible catalytic effects were shown for desorption kinetics suggesting a small catalytic effect on oxygen adsorption. The high humidity effect on sensing performance was also studied.

CRediT authorship contribution statement

Nguyen Manh Hung: Conceptualization, Methodology, Writing - original draft. **Nguyen Minh Hieu:** Data curation, Methodology. **Nguyen Duc Chinh:** Data curation, Methodology. **Truong Thi Hien:** Methodology. **Nguyen Duc Quang:** Methodology. **Sutripto Majumder:** Methodology. **GyuSeok Choi:** . **Chunjoong Kim:** Supervision, Writing - review & editing. **Dojin Kim:** Supervision, Writing - review & editing, Project administration, Funding acquisition.

Declaration of Competing Interest

We have no competing interests to declare regarding our manuscript, which is submitted to the Sensors and actuators B.

Acknowledgements

This work was supported by the National Research Lab program (NRF-2018R1A2A1A05023126) of the National Research Foundation of Korea.

Appendix A. Supplementary data

Supplementary material related to this article can be found, in the online version, at doi:https://doi.org/10.1016/j.snb.2020.128001.

References

[1] M.-T. Ke, M.-T. Lee, C.-Y. Lee, L.-M. Fu, A MEMS-based benzene gas sensor with a self-heating WO3 sensing layer, Sensors 9 (2009) 2895–2906.
[2] C.-Y. Lee, C.-M. Chiang, Y.-H. Wang, R.-H. Ma, A self-heating gas sensor with integrated NiO thin-film for formaldehyde detection, Sens. Actuators, B: Chem. 122 (2007) 503-10 %@ 0925-4005.
[3] B. Urasinska-Wojcik, T.A. Vincent, M.F. Chowdhury, J.W. Gardner, Ultrasensitive WO3 gas sensors for NO2 detection in air and low oxygen environment, Sens. Actuators, B: Chem. 239 (2017) 1051–1059 %@ 0925-4005.
[4] N. Van Hoang, C.M. Hung, N.D. Hoa, N. Van Duy, N. Van Hieu, Facile on-chip electrospinning of ZnFe2O4 nanofiber sensors with excellent sensing performance to H2S down ppb level, J. Hazard. Mater. 360 (2018) 6–16 %@ 0304-3894.
[5] R. Lu, X. Zhong, S. Shang, S. Wang, M. Tang, Effects of sintering temperature on sensing properties of WO_3 and Ag-WO_3 electrode for NO_2 sensor, R. Soc. Open Sci. 5 (2018) 171691.
[6] Y.-D. Wang, L.-F. Yang, Z.-L. Zhou, Y.-F. Li, X.-H. Wu, Effects of calcining temperature on lattice constants and gas-sensing properties of Nb2O5, Mater. Lett. 49 (2001) 277–281 %@ 0167-577X.
[7] R. Dhahri, M. Hjiri, L.E. Mir, A. Bonavita, D. Iannazzo, S. Leonardi, et al., CO sensing properties under UV radiation of Ga-doped ZnO nanopowders, Appl. Surf. Sci. 355 (2015) 1321–1326.
[8] L. Han, D. Wang, Y. Lu, T. Jiang, L. Chen, T. Xie, et al., Influence of annealing temperature on the photoelectric gas sensing of Fe-doped ZnO under visible light irradiation, Sens. Actuators B 177 (2013) 34–40.
[9] Y. Hou, A.H. Jayatissa, Effect of laser irradiation on gas sensing properties of sol–gel derived nanocrystalline Al-doped ZnO thin films, Thin Solid Films 562 (2014) 585–591.
[10] J. Zhai, L. Wang, D. Wang, Y. Lin, D. He, T. Xie, UV-illumination room-temperature gas sensing activity of carbon-doped ZnO microspheres, Sens. Actuators B 161 (2012) 292–297.
[11] D. Haridas, A. Chowdhuri, K. Sreenivas, V. Gupta, Enhanced room temperature response of SnO2 thin film sensor loaded with Pt catalyst clusters under UV radiation for LPG, Sens. Actuators B 153 (2011) 152–157.
[12] D. Haridas, V. Gupta, Study of collective efforts of catalytic activity and photoactivation to enhance room temperature response of SnO2 thin film sensor for methane, Sens. Actuators B 182 (2013) 741–746.
[13] Y. Li, J. Gong, G. He, Y. Deng, Enhancement of photoresponse and UV-assisted gas sensing with Au decorated ZnO nanofibers, Mater. Chem. Phys. 134 (2012) 1172–1178.
[14] G. Lu, J. Xu, J. Sun, Y. Yu, Y. Zhang, F. Liu, UV-enhanced room temperature NO2 sensor using ZnO nanorods modified with SnO2 nanoparticles, Sens. Actuators B 162 (2012) 82–88.
[15] D. Ao, M. Ichimura, UV irradiation effects on hydrogen sensors based on SnO2 thin films fabricated by the photochemical deposition, Solid-State Electron. 69 (2012) 1–3.
[16] B. de Lacy Costello, R. Ewen, N.M. Ratcliffe, M. Richards, Highly sensitive room temperature sensors based on the UV-LED activation of zinc oxide nanoparticles, Sens. Actuators B 134 (2008) 945–952.
[17] L. Peng, Q. Zhao, D. Wang, J. Zhai, P. Wang, S. Pang, et al., Ultraviolet-assisted gas sensing: a potential formaldehyde detection approach at room temperature based on zinc oxide nanorods, Sens. Actuators B 136 (2009) 80–85.
[18] J.D. Prades, R. Jiménez-Díaz, F. Hernandez-Ramirez, S. Barth, A. Cirera, A. Romano-Rodriguez, et al., Equivalence between thermal and room temperature UV light-modulated responses of gas sensors based on individual SnO2 nanowires, Sens. Actuators B 140 (2009) 337–341.
[19] A. Soleimanpour, Y. Hou, A.H. Jayatissa, The effect of UV irradiation on nanocrystalline zinc oxide thin films related to gas sensing characteristics, Appl. Surf. Sci. 257 (2011) 5398–5402.
[20] C. Zhang, A. Boudiba, P. De Marco, R. Snyders, M.-G. Olivier, M. Debliquy, Room temperature responses of visible-light illuminated WO3 sensors to NO2 in sub-ppm range, Sens. Actuators B 181 (2013) 395–401.
[21] Y. Zhou, C. Gao, Y. Guo, UV assisted ultrasensitive trace NO 2 gas sensing based on few-layer MoS 2 nanosheet–ZnO nanowire heterojunctions at room temperature, J. Mater. Chem. A Mater. 6 (2018) 10286–10296.
[22] Y. Zhou, X. Li, Y. Wang, H. Tai, Y. Guo, UV illumination-enhanced molecular ammonia detection based on a ternary-reduced graphene oxide–titanium dioxide–Au composite film at room temperature, Anal. Chem. 91 (2018) 3311–3318.
[23] N.D. Chinh, T.T. Hien, L. Do Van, N.M. Hieu, N.D. Quang, S.-M. Lee, et al., Adsorption/desorption kinetics of nitric oxide on zinc oxide nano film sensor enhanced by light irradiation and gold-nanoparticles decoration, Sens. Actuators, B: Chem. 281 (2019) 262–272 %@ 0925-4005.
[24] N.D. Chinh, N.D. Quang, H. Lee, T. Thi Hien, N.M. Hieu, D. Kim, et al., NO gas sensing kinetics at room temperature under UV light irradiation of In_2O_3 nanostructures, Sci. Rep. 6 (2016) 35066.
[25] L. Han, D. Wang, J. Cui, L. Chen, T. Jiang, Y. Lin, Study on formaldehyde gas-sensing of In_2O_3-sensitized ZnO nanoflowers under visible light irradiation at room temperature, J. Mater. Chem. 22 (2012) 12915–12920.
[26] S. Trocino, P. Frontera, A. Donato, C. Busacca, L.A. Scarpino, P. Antonucci, et al., Gas sensing properties under UV radiation of In2O3 nanostructures processed by electrospinning, Mater. Chem. Phys. 147 (2014) 35–41 %@ 0254-584.
[27] T. Wagner, C.-D. Kohl, C. Malagù, N. Donato, M. Latino, G. Neri, et al., UV light-enhanced NO_2 sensing by mesoporous In_2O_3: interpretation of results by a new

sensing model, Sens. Actuators B 187 (2013) 488–494.
[28] W. Zang, Y. Nie, D. Zhu, P. Deng, L. Xing, X. Xue, Core–shell In2O3/ZnO nanoarray nanogenerator as a self-powered active gas sensor with high H2S sensitivity and selectivity at room temperature, J. Phys. Chem. C 118 (2014) 9209–9216 %@ 1932-7447.
[29] H. Yamaura, T. Jinkawa, J. Tamaki, K. Moriya, N. Miura, N. Yamazoe, Indium oxide-based gas sensor for selective detection of CO, Sens. Actuators, B: Chem. 36 (1996) 325–332 %@ 0925-4005.
[30] N.M. Vuong, N.M. Hieu, H.N. Hieu, H. Yi, D. Kim, Y.-S. Han, et al., Ni2O3-decorated SnO2 particulate films for methane gas sensors, Sens. Actuators, B: Chem. 192 (2014) 327–333.
[31] N.D. Chinh, N.D. Quang, H. Lee, T.T. Hien, N.M. Hieu, D. Kim, et al., NO gas sensing kinetics at room temperature under UV light irradiation of In 2 O 3 nanostructures, Sci. Rep. 6 (2016) 35066 %@ 2045-2322.
[32] J.M. Kim, J.K. Park, K.N. Kim, C.H. Kim, H.G. Jang, Synthesis of In2O3 nano-materials with various shapes, Curr. Appl Phys. 6 (2006) e198–e201 %@ 1567-739.
[33] N.M. Vuong, D. Kim, H. Kim, Surface gas sensing kinetics of a WO3 nanowire sensor: part 1—oxidizing gases, Sens. Actuators, B: Chem. 220 (2015) 932–941 %@ 0925-4005.
[34] N.M. Vuong, D. Kim, H. Kim, Surface gas sensing kinetics of a WO3 nanowire sensor: part 2—Reducing gases, Sens. Actuators, B: Chem. 224 (2016) 425–433.
[35] S. Dash, Z. Singh, S.C. Parida, V. Venugopal, Thermodynamic studies on Rb2ThO3(s), J. Alloys Compd. 398 (2005) 219–227.
[36] C. Kranert, R. Schmidt-Grund, M. Grundmann, Raman active phonon modes of cubic In_2O_3, Phys. Stat. Sol. RRL 8 (2014) 554–559.
[37] D. Liu, W. Lei, S. Qin, L. Hou, Z. Liu, Q. Cui, et al., Large-scale synthesis of hexagonal corundum-type In_2O_3 by ball milling with enhanced lithium storage capabilities, J. Mater. Chem. A Mater. 1 (2013) 5274–5278.
[38] N. Koura, S. Kohara, K. Takeuchi, S. Takahashi, L. Curtiss, M. Grimsditch, et al., Alkali carbonates: Raman spectroscopy, ab initio calculations, and structure, J. Mol. Struct. 382 (1996) 163–169.
[39] J.F. Moulder, Handbook of X-ray photoelectron spectroscopy, Phys. Electron. (1995) 230–232.
[40] N. Yamazoe, J. Tamaki, N. Miura, Role of hetero-junctions in oxide semiconductor gas sensors, Mater. Sci. Eng. B 41 (1996) 178–181.
[41] P. Patnaik, Handbook of Inorganic Chemicals, McGraw-Hill, 2002.
[42] G.C. Xie, L. Fanga, L.P. Peng, G.B. Liu, H.B. Ruan, F. Wu, et al., Effect of In-doping on the optical constants of ZnO thin films, Phys. Procedia 32 (2012) 651–657.
[43] Q. Geng, Z. He, X. Chen, W. Dai, X. Wang, Gas sensing property of ZnO under visible light irradiation at room temperature, Sens. Actuators B 188 (2013) 293–297.
[44] N.D. Chinh, C. Kim, D. Kim, UV-light-activated H2S gas sensing by a TiO2 nanoparticulate thin film at room temperature, J. Alloys Compd. 778 (2019) 247–255 % @ 0925-8388.
[45] N.M. Hieu, C.V. Phuoc, T.T. Hien, N.D. Chinh, N.D. Quang, C. Kim, et al., A separated receptor/transducer scheme as strategy to enhance the gas sensing performance using Hematite–carbon nanotube composite, Sensors 19 (2019) 3915.
[46] A. Ayeshamariam, M. Bououdina, C. Sanjeeviraja, Optical, electrical and sensing properties of In_2O_3 nanoparticles, Mater. Sci. Semicond. Process. 16 (2013) 686–695.
[47] M.M. Khan, W. Khan, M. Ahamed, M. Alhoshan, Structural and optical properties of In_2O_3 nanostructured thin film, Mater. Lett. 79 (2012) 119–121.
[48] P. King, T.D. Veal, F. Fuchs, C.Y. Wang, D. Payne, A. Bourlange, et al., Band gap, electronic structure, and surface electron accumulation of cubic and rhombohedral In_2O_3, Phys. Rev. B 79 (2009) 205211.
[49] K. Boulenouar, Mh. Bouslama, A. Mokadem, Sb. Vizzini, Z. Lounis, A. Abdellaoui, et al., Auger electron spectroscopy, electron energy loss spectroscopy, UV photoelectron spectroscopy, and photoluminescence characterization of In2O3 associated to the theoretical calculations based on the generalized gradient approximation and modified Becke Johnson, J. Phys. Chem. C 121 (2017) 8345–8352.
[50] E. Comini, G. Faglia, G. Sberveglieri, UV light activation of tin oxide thin films for NO2 sensing at low temperatures, Sens. Actuators, B: Chem. 78 (2001) 73–77.
[51] S. Park, S. An, Y. Mun, C. Lee, UV-enhanced NO2 gas sensing properties of SnO2-core/ZnO-shell nanowires at room temperature, ACS Appl. Mater. Interfaces 5 (2013) 4285–4292.
[52] F.H. Saboor, T. Ueda, K. Kamada, T. Hyodo, Y. Mortazavi, A.A. Khodadadi, et al., Enhanced NO2 gas sensing performance of bare and Pd-loaded SnO2 thick film sensors under UV-light irradiation at room temperature, Sens. Actuators, B 223 (2016) 429–439.
[53] S. Moon, N.M. Vuong, D. Lee, D. Kim, H. Lee, D. Kim, et al., Co3O4–SWCNT composites for H2S gas sensor application, Sens. Actuators, B: Chem. 222 (2016) 166–172.
[54] N. Barsan, U. Weimar, Conduction model of metal oxide gas sensors, J. Electroceram. 7 (2001) 143–167.
[55] G. Rubasinghege, V.H. Grassian, Role (s) of adsorbed water in the surface chemistry of environmental interfaces, Chem. Commun. 49 (2013) 3071–3094.
[56] J. Baltrusaitis, J. Schuttlefield, J.H. Jensen, V.H. Grassian, FTIR spectroscopy combined with quantum chemical calculations to investigate adsorbed nitrate on aluminium oxide surfaces in the presence and absence of co-adsorbed water, Phys. Chem. Chem. Phys. 9 (2007) 4970–4980.

Nguyen Manh Hung received his master of materials science in Hanoi University of Science and Technology (HUST), Vietnam, in 2016. Currently, he is a PhD candidate in the Department of Materials Science and Engineering, Chungnam National University, Republic of Korea. His current research interests include nanomaterials, nanofabrication and applications to PEC water splitting and gas sensor, especially low-temperature gas sensor.

Nguyen Minh Hieu received his master of materials science in Chungnam National University (CNU), Rep. of Korea, in 2014. He is a PhD candidate in the Department of Materials Science and Engineering, Chungnam National University, Rep of Korea. His current research interests include nanomaterials, nanofabrication and application to gas sensors, especially room temperature gas detector.

Nguyen Duc Chinh received his PhD in materials science and engineering at Chungnam Nat. Univ., Korea in 2019. He is now at a post doctor in Nano Materials and Application Lab. at Chungnam Nat. Univ. His current interests include nanomaterials, nanofabrication, and their applications to electronic devices: gas sensor and photoelectrochemical water splitting.

Truong Thi Hien received her PhD in materials science and engineering at Chungnam Nat. Univ., Korea in 2019. Her current interests are nano structure materials and their applications to photoelectrochemical systems.

Nguyen Duc Quang received his master degree from the Department of Materials Science and Engineering, Chungnam National University, Korean, in 2016. Currently, he is in Ph.D course in the Department of Materials Science and Engineering, CNU. His current research focus on nanomaterials, nanofabrication, and their applications to photocatalytic and photo water splitting.

Sutripto Majumder received his Ph.D. in Department of Physics at Visvesvaraya National Institute of Technology (VNIT), Nagpur (India) in 2017. Recently, he is working as a postdoctoral fellow in Nano Materials and Application Lab. at Chungnam National University, Republic of Korea. His current research interest is synthesis and fabrication of nanostructured thin films electrodes for photoelectrochemical water splitting and solar cells.

GyuSeok Choi received his PhD in Materials Science and Engineering at Chungnam Nat. Univ., KOREA in 2003. He is a Director of Gumi Electronic Research Institute, Korea. His current research interests are nanomaterial synthesis and applications to electronic and energy devices including batteries, displays, wearable devices.

Chunjoong Kim received his Ph.D. degree in Materials Science and Engineering of Seoul National University, Korea. He is currently an associate professor in the Department of Materials Science and Engineering at Chungnam National University since 2015. His current research interests include the understanding of reaction mechanism in the materials for energy storage devices, photoelectrochemical cells, sensors.

Dojin Kim received his PhD in Materials Science and Engineering at University of Southern California, USA in 1989. He is a professor of Department of Materials Science and Engineering at Chungnam Nat. Univ., Korea since 1992. His current research interests are nanostructures synthesis and applications to electronic and energy devices including gas and bio sensors, displays, transparent conducting films, electrodes for photoelectrochemical cells and solar cells.